



OPEN

# Study of the mechanical characteristics of coal-serial sandstone after high temperature treatment under true triaxial loading

Shuai Wang, Lianguo Wang<sup>✉</sup>, Bo Ren, Ke Ding, Chongyang Jiang & Jiaying Guo

In this study, a series of true triaxial loading tests were carried out on coal-measure sandstone after high temperature treatment by using a self-developed true triaxial test system combined with acoustic emission (AE) monitoring, and the mass loss, deformation characteristics and loss failure mode of sandstone before and after heat treatment were systematically studied. It is found that the true triaxial mechanical properties of sandstone after high temperature treatment are closely related to temperature, and the peak strength, maximum principal strain, volume strain, minimum fracture angle and elastic modulus, which all showed bimodal changes, and 800 °C is the threshold temperature of the first four parameters. The transition temperature of the elastic modulus is 400 °C. It is found that the test results of true triaxial high temperature sandstone are in good agreement with the existing true triaxial theory and test results. The failure forms of the samples at different temperatures show inverted “Y” or inverted “N” shapes. Shear failure occurs when the temperature is below 400 °C, and shear-tension failure occurs when the temperature is above 600 °C. At the same time, it is found that the AE signal has four periods, namely the quiet period, growth period, explosion period and decline period. The number of AE events corresponds to the deviatoric stress interval well. Experimental study of the mechanical properties of sandstone under the coupling effect of high temperature and true triaxial stress has guiding significance for the parameter selection and safety evaluation of roof sandstone in underground coal gasification.

Due to engineering factors such as the deep-formation disposal of high-level radioactive nuclear waste<sup>1,2</sup>, underground coal gasification and storage<sup>3–6</sup>, and the development of geothermal resources<sup>7,8</sup>, the management of rock-engineering problems in high temperature environments has become an important area of research. Influenced by the composition, microstructure and macrostructure, the physical and mechanical properties of rocks often change significantly after experiencing high temperatures. Because underground rock-engineering activities are usually carried out under true triaxial stress<sup>9,10</sup>, it is very important to study the strength, damage and failure behavior of rocks under true triaxial stress to accurately predict and evaluate the stability of underground rock engineering.

There are many differences in the mineral composition of rocks due to the physical and chemical processes involved in diagenesis. The thermal expansion rate of different mineral particles is different. Under the action of the thermal load, microcracks will close, expand, and condense in rock samples<sup>11–13</sup>. To date, scholars at home and abroad have carried out extensive research on the physical properties of high-temperature-treated sandstone, and achieved fruitful results. The researchers found changes in the thermal properties of the high-temperature-treated sandstone, including the mineral composition<sup>14,15</sup>, porosity<sup>16,17</sup>, wave velocity<sup>18,19</sup>, and thermal conductivity<sup>20</sup>. These changes affect the physical and mechanical properties of rocks, so it is important to further understand the thermal damage behavior of rocks.

The real-time physical and mechanical properties testing of rocks at a high temperature is limited by the availability of equipment. Therefore, scholars usually treat rocks with a high temperature first, and wait for the temperature to drop to normal temperatures before conducting various tests. Additionally, researchers have

State Key Laboratory for Geomechanics and Deep Underground Engineering, China University of Mining and Technology, Xuzhou 221116, China. ✉email: cumt\_lgwang@163.com

carried out laboratory mechanical tests on high-temperature sandstone. Uniaxial compression tests<sup>21–24</sup>, Brazilian splitting tests<sup>25,26</sup>, shear tests<sup>27</sup> and conventional triaxial tests<sup>28,29</sup> were carried out to test compression strength, tensile strength, peak strain, elastic modulus, Poisson's ratio, cohesion, the internal friction Angle and other parameters of high-temperature-treated sandstone, and to discuss the correlation between stress and high temperatures. There are different views in the research of temperature thresholds. Some scholars believe that major changes in rock strength usually occur at above 600 °C<sup>30,31</sup>, while others believe that the rock structure will also soften when the temperature is 500–600 °C<sup>32,33</sup>. It was found that these changes were mainly attributed to the transformation of the crystal structure, mineral decomposition, and water loss<sup>34,35</sup>. For sedimentary rocks such as sandstone, the coefficient of thermal expansion mainly depends on its mineral composition; for example, a higher occurrence of damage is likely under high temperatures when the rock contains higher levels of calcite<sup>36</sup>. The physical and mechanical properties of some sandstones after heat treatment are summarized in Table 1.

To be able to characterize the progressive rupture behavior of high-temperature sandstone triaxial tests, researchers have investigated sandstone damage by means of acoustic emission<sup>38,39</sup>, CT radiography<sup>40</sup>, infrared thermography<sup>41</sup> and nuclear magnetic resonance techniques<sup>42</sup>. However, the existing research on the damage evolution and failure behavior of high temperature sandstone mainly focuses on uniaxial compression<sup>43</sup>, conventional triaxial states, and the Brazilian splitting test. The deformation characteristics, strength characteristics, and acoustic emission monitoring law of high temperature rocks under true triaxial tests (TTT) require further investigation. The origin of the true triaxial tests can be traced back to 1971, since Mogi<sup>9</sup> developed the world's first true triaxial test machine, which opened the prelude to the true triaxial test and proposed the octahedral strength criterion for rocks, Haimson et al.<sup>44–46</sup> further discovered the effect of intermediate principal stress on specimens, Al-Ajmi et al.<sup>47,48</sup> found a better fit for the linear octahedral strength criterion by collating a large amount of true triaxial data, and called their strength criterion the Mogi-Coulomb criterion.

The aim of this study is to reveal the intrinsic mechanism of temperature effects on rock strength. Firstly, the effect of temperature on the physical and mechanical properties of sandstone was analyzed. The mineral composition of coal-serial sandstone was analyzed using X-ray diffraction (XRD) method. Secondly, true triaxial loading tests were carried out on sandstone samples subjected to high temperatures using a self-developed true three-axis electro-hydraulic servo loading test system<sup>49</sup>, and the causes and regularity of changes in the mechanical parameters of sandstone following high-temperature treatment were analyzed. During the tests, an acoustic emission monitoring system was used to capture the damage evolution and failure process of sandstone in real time<sup>50</sup>. The aim of this paper is to provide a scientific basis for predicting and evaluating the stability and safety of underground engineering, a high-temperature sandstone roof for underground coal gasification.

## Rock sample preparation and test methods

**Experiential materials.** The experimental rock samples are taken from the roof sandstone of the Taiyuan Formation–Shanxi Formation coal seam in Ordos Basin, and the rock mass is hard and compact<sup>15</sup>. The sampling position of the test rock sample is shown in Fig. 1. The rock formation is at 950–1020 m below ground. Macroscopically, the hue of sandstone at NT is gray, and the outer surface is smooth without obvious holes, joints or macroscopic cracks. The results of X-ray diffraction analysis revealed that the rock samples were feldspar quartz sandstone, containing 44% quartz, 35% feldspar minerals, 10% clay minerals, 7% calcite, and 4% zeolite<sup>51</sup> (as shown in Fig. 2). According to the requirements of the test platform, the processed rock sample is a rectangular specimen with length, width and height of about 50 mm × 50 mm × 100 mm. The average density of the sample at normal temperature (NT) is 2620 kg/m<sup>3</sup>. According to field studies on underground coal gasification, the use of non-well, reverse ignition results in the formation of a void known as the gasification chamber, where a combustion zone is formed. The temperature of the flame working face can normally reach 800–1200 (°C) during gasification. The thermal energy in the working face can be transferred to surrounding rock through thermal conduction, convection, and radiation, resulting in changes in the temperature field within surrounding rock<sup>52</sup>. Based on different experimental temperatures, the samples were divided into six groups (a total of 24 sandstone specimens, with an additional six specimens). In order to analyze and compare the effects of temperature on the micro-damage of the sandstone, scanning electron microscopy was used to observe the micrographs of the sandstone specimens after exposure to high temperatures.

| Ref                          | Site                                | Max. temp. achieved (°C) | Measurement condition | Main mineral   | Tested properties   |
|------------------------------|-------------------------------------|--------------------------|-----------------------|--|---|
| Ranjith et al. <sup>22</sup> | Gosford, New South Wales, Australia | 950                      | Cooled down           | Quartz, Kaolinite, Illite  | UCS, Elastic modulus  |
| Zhang et al. <sup>32</sup>   | Xuzhou, China                       | 800                      | Heating process       | –  | UCS, Elastic modulus  |
| Hajpál <sup>18</sup>         | German and Hungarian                | 900                      | Cooled down           | Quartz, Feldspar, Micas, Clay minerals (Kaolinite, Chlorite, Glauconite) | Density, Porosity, Water adsorption, Ultrasonic sound velocity, Duroskop rebound, UCS and Indirect tensile strength |
| Sun et al. <sup>20</sup>     | Linyi, China                        | 900                      | Cooled down           | Quartz, Feldspar, Dolomite/Ankerite, Hematite/Magnetite                  | Thermal conductivity, Thermal diffusivity, Heat capacity  |
| Lei et al. <sup>21</sup>     | Chongqing, China                    | 900                      | Cooled down           | Quartz, Feldspar, Plagioclase, Clayminerals                              | Mass, Volume, Density, Poisson's ratio, Elastic modulus, UCS  |
| Mahanta et al. <sup>37</sup> | Rajasthan, India                    | 900                      | Cooled down           | Quartz, Dickite, Kaolinite, Calcite                                      | UCS, Tensile strength, Elastic modulus, Poisson's ratio   |

**Table 1.** Effect of thermal treatment on the physical and mechanical properties of sandstone: insights.

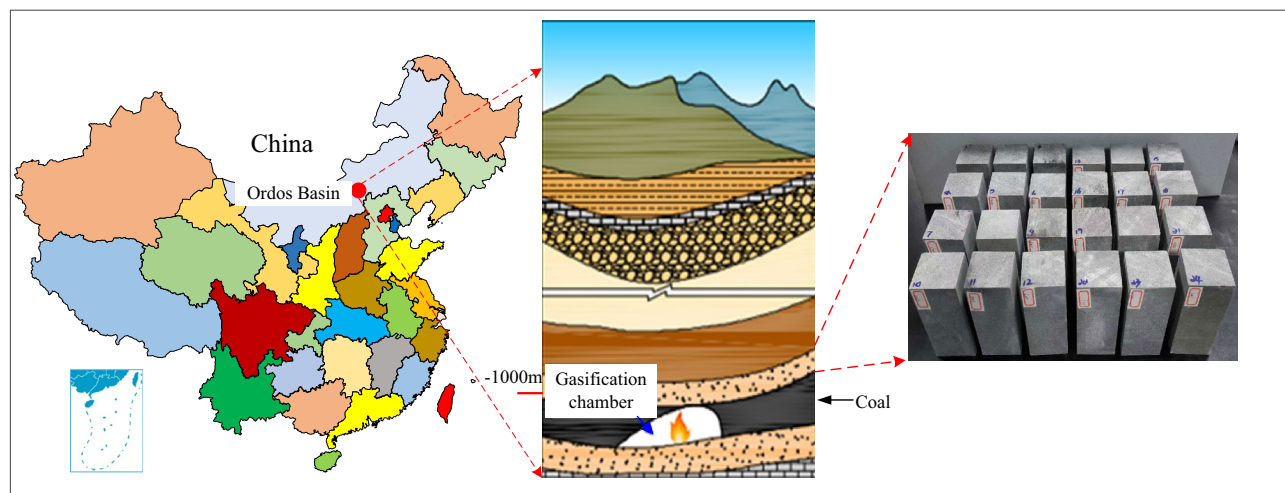


**Figure 1.** Schematic diagram of the sandstone sampling location.

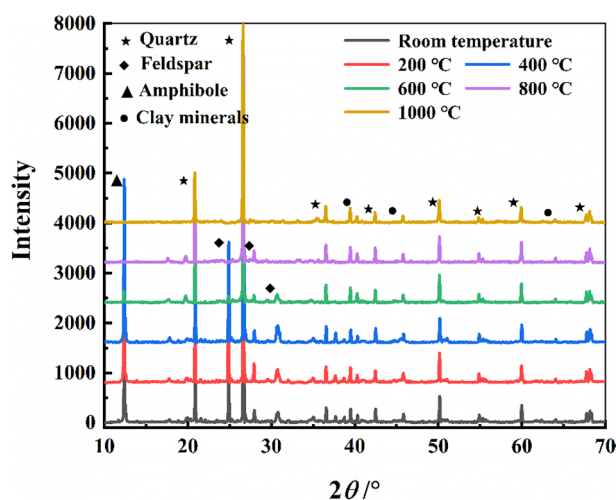


**Figure 2.** XRD analysis of sandstone.

**Experimental equipment.** *MXQ1700 box type atmosphere furnace.* MXQ1700 box-type atmosphere ovens<sup>15</sup> (produced by Shanghai Weixing Machinery Equipment Co., Ltd., China) use a Japanese SMC digital display pressure gauge, which has high temperature control accuracy, a temperature control accuracy of 1 °C, average temperature in the oven of 5 °C, and the highest heating temperature can reach 1700 °C. At the same time, the equipment has a built-in water cooling system and vacuum system, and the vacuum degree can reach 0.1 MPa. It can meet the high-temperature heating requirements of sandstone on the roof of deep underground coal gasification coal seam.

*True triaxial electro-hydraulic servo loading test system.* This test was conducted on a self-developed rock true triaxial electro-hydraulic servo loading test system, which mainly comprised a triaxial servo control loading system, a true triaxial pressure chamber, and an automatic acquisition system (Fig. 3)<sup>49,53</sup>.

**Experimental process.** *Heating process of sample.* The heating curve of the sample is shown in Fig. 4. Following high-temperature treatment, the rock samples change from gray to brown-red, and the color gradually deepens with the increase in temperature; however, the sandstone samples at 1000 °C become dark and produce transverse cracks perpendicular to the height direction. The rock sample grouping and basic parameters are shown in Table 2.

*Loading test scheme.* The deep rock mass is in a three-dimensional unequal compressive stress state. In order to simulate a more realistic stress environment, the loading scheme is shown in Fig. 4. The specific steps are described in the following (Fig. 5)<sup>54</sup>.

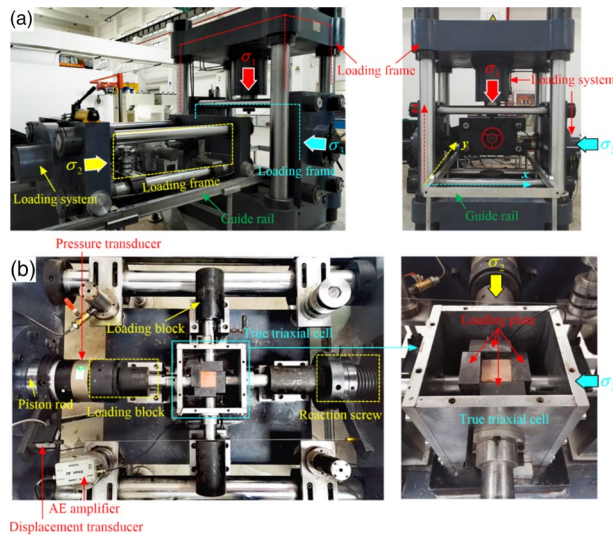


Figure 3. True triaxial compression test system<sup>49</sup>.

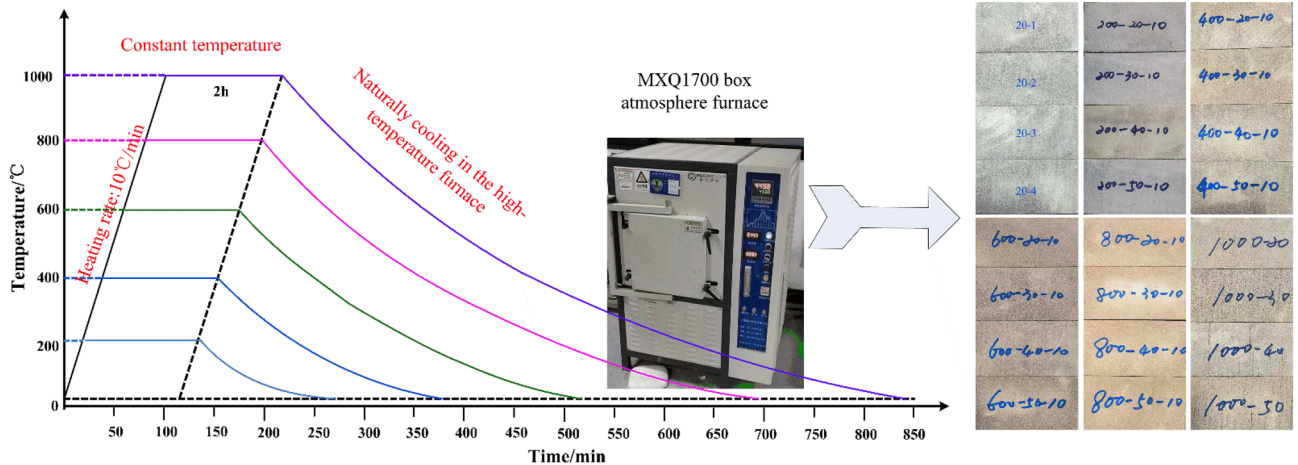


Figure 4. Curves of sandstone samples in the heat treatment<sup>15</sup>.

- (1) Apply a certain preload to fully fix the sample, and then apply the confining pressure to the hydrostatic pressure state at a rate of 0.04 MPa/s. At this time,  $\sigma_1 = \sigma_2 = \sigma_3 = 10$  MPa.
- (2) With  $\sigma_3$  kept unchanged, continue to increase  $\sigma_1$  and  $\sigma_2$  at the same rate to 20 MPa.
- (3) With  $\sigma_2$  and  $\sigma_3$  kept unchanged, increase  $\sigma_1$  at a rate of 0.004 mm/s according to the displacement loading method until the sample fails. During the test, the AE activities are recorded in real-time.

## Results

**Analysis on deformation characters.** The stress–strain curve plays a crucial role in understanding the mechanical behavior, deformation characteristics, and strength properties of sandstone specimens. The stress–strain curves of sandstone samples under the true triaxial loading stress paths are illustrated in Fig. 6. In a three-dimensional stress state, the deformation of an object can be described by three principal strains, denoted as  $\epsilon_1$ ,  $\epsilon_2$ , and  $\epsilon_3$ , which represent the deformations occurring along the three principal strain directions.

The true triaxial stress–strain curve of the sandstone exhibits four typical stages, namely the upward concave segment, linear segment, downward bending slope segment, and post-peak strain softening stage. Within the temperature range of room temperature to 800 °C, there is a significant stress reduction after the peak, indicating that the sandstone in the underlying formation still exhibits a strong brittle behavior. When the temperature increases to 1000 °C, the sample undergoes less stress reduction after the peak. The sandstone sample shows a clear trend of plastic flow.

The relationship curves between deviatoric stress and the three principal strains in sandstone exhibit similarities under different temperatures. All curves demonstrate non-linear characteristics. Due to the different true triaxial stress states,  $\sigma_3$  is the smallest; therefore, the strain in that direction (minimum principal strain  $\epsilon_3$ )

| Sample temperature | Sample no | Length/mm | Width/mm | Height/mm | Weight/g       |               | Mass loss/g |
|--------------------|-----------|-----------|----------|-----------|----------------|---------------|-------------|
|                    |           |           |          |           | Before heating | After heating |             |
| NT                 | SD-20-1   | 49.8      | 50.1     | 100.1     | 644            | 644           | 0           |
|                    | SD-20-2   | 49.9      | 49.9     | 100.2     | 647            | 647           |             |
|                    | SD-20-3   | 50.2      | 50.1     | 99.9      | 651            | 651           |             |
| 200 °C             | SD-200-1  | 50.0      | 50.1     | 100.0     | 645            | 641           | 3.67        |
|                    | SD-200-2  | 50.1      | 50.0     | 100.1     | 648            | 644           |             |
|                    | SD-200-3  | 49.9      | 49.8     | 100.0     | 651            | 648           |             |
| 400 °C             | SD-400-1  | 49.8      | 50.0     | 100.1     | 645            | 642           | 4.33        |
|                    | SD-400-2  | 49.8      | 49.9     | 99.9      | 648            | 642           |             |
|                    | SD-400-3  | 49.7      | 50.1     | 100.1     | 654            | 650           |             |
| 600 °C             | SD-600-1  | 49.8      | 50.0     | 100.2     | 646            | 632           | 13.33       |
|                    | SD-600-2  | 49.9      | 50.1     | 100.1     | 648            | 635           |             |
|                    | SD-600-3  | 49.8      | 50.2     | 99.8      | 657            | 644           |             |
| 800 °C             | SD-800-1  | 49.9      | 49.9     | 100.0     | 646            | 614           | 30.33       |
|                    | SD-800-2  | 49.8      | 49.9     | 100.1     | 648            | 620           |             |
|                    | SD-800-3  | 49.9      | 49.9     | 100.2     | 657            | 626           |             |
| 1000 °C            | SD-1000-1 | 50.0      | 50.1     | 100.1     | 647            | 597           | 48.67       |
|                    | SD-1000-2 | 50.1      | 50.1     | 100.1     | 649            | 606           |             |
|                    | SD-1000-3 | 50.1      | 50.2     | 100.2     | 658            | 605           |             |

**Table 2.** Physical parameters of rock samples.

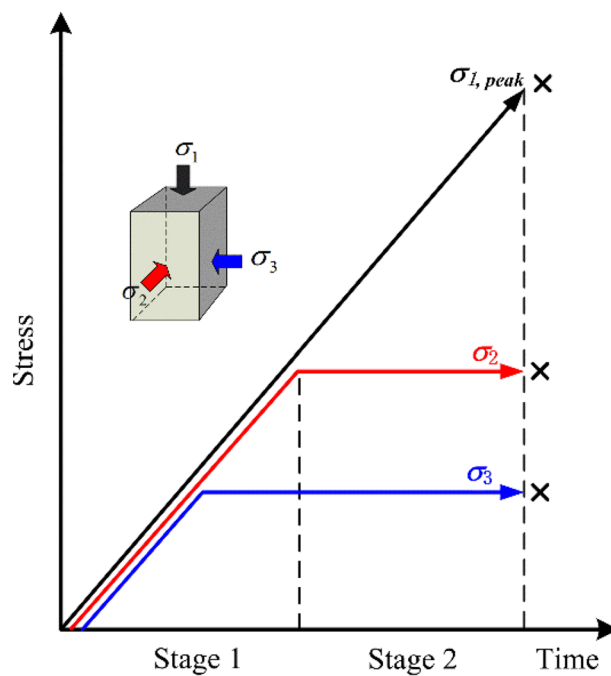


**Figure 5.** Schematic diagram of loading stress paths.

exhibits expansive deformation characteristics. The post-peak stage is entirely characterized by softening, and when the temperature increases to 1000 °C, the maximum principal strain shows a post-peak plastic flow trend.

In conclusion, all instances of the failure of sandstone samples in the range of NT to 800 °C show sudden brittle failure located at the peak stress point. When the temperature reaches 1000 °C, the ductility of the sandstone specimens is enhanced, there is no sudden stress drop, and a plastic flow trend is observed.

In order to better analyze the influence of temperature on deformation characteristics, the relationship between principal strain and temperature is obtained, as shown in Fig. 7. A positive value indicates compressive deformation, while a negative value indicates expansion deformation. The peak strain refers to the maximum strain reached by a material under loading or stress. In true triaxial tests, since there are three principal directions, three peak strain values will be obtained for each direction. The peak strain ( $\epsilon_1$  direction) exhibits a "bimodal"



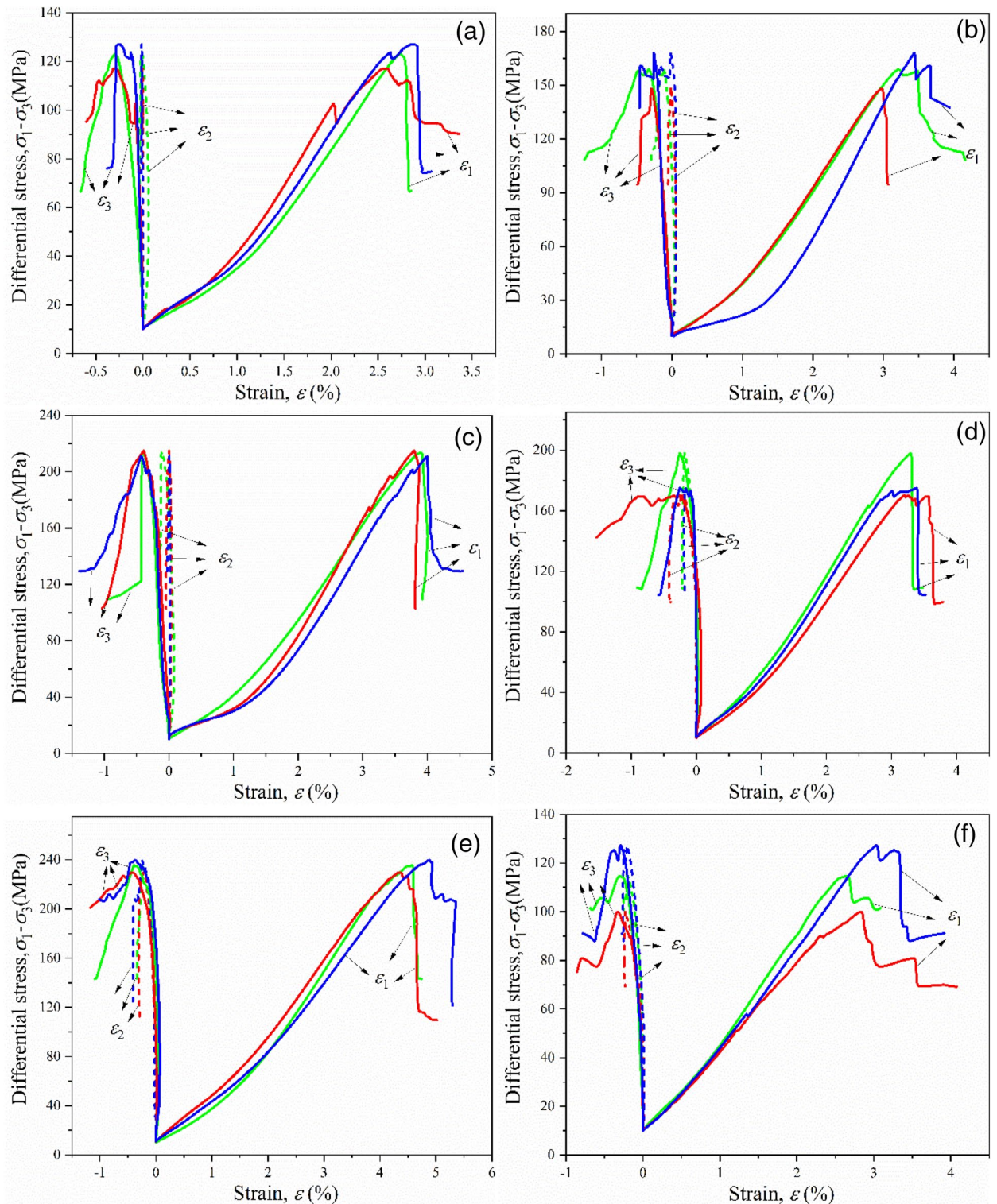


**Figure 6.** The relationship between deviatoric stress and the three principal strains under true triaxial conditions is shown. Each color represents a single experiment, and figures (a)–(f) represent the experimental data at six different temperatures.

pattern with increasing temperature (Fig. 7a). The maximum principal strain is the most significant and plays a decisive role in the three principal stress directions. When the temperature rises from NT to 400 °C, the maximum principal strain increases from 2.74 to 3.90%, representing an increase of 42.3%. From 400 to 600 °C, the maximum principal strain of sandstone decreases from 3.90 to 3.23%, with a decrease of 17.2%. When the temperature ranges from 600 to 800 °C, the maximum principal strain of sandstone increases from 3.23 to 4.58%, with an increase of 41.8%. When the temperature ranges from 800 to 1000 °C, the maximum principal strain of

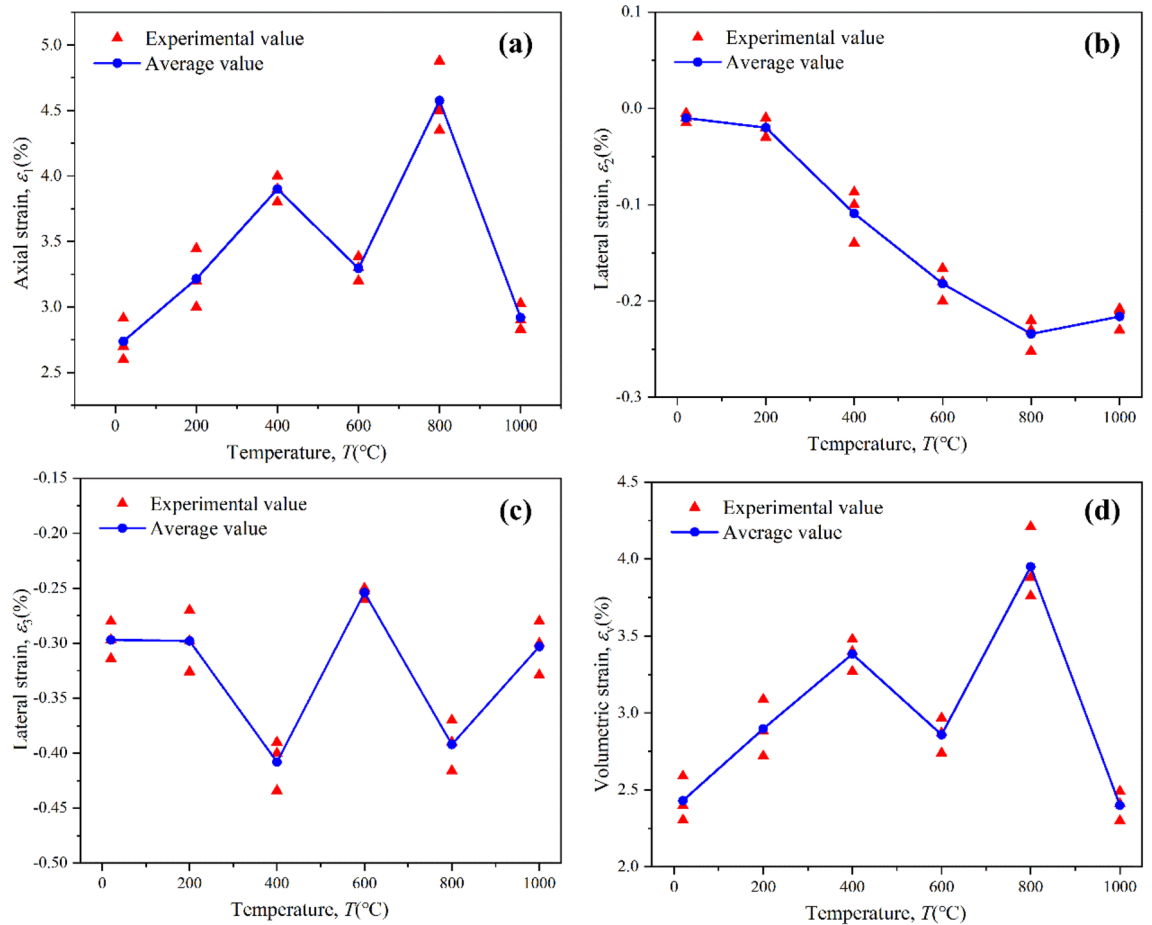


**Figure 7.** The variation of principal strain with temperature under true triaxial conditions; (a) maximum principal strain; (b) intermediate principal strain; (c) minimum principal strain; and (d) volumetric strain.

sandstone drops sharply from 4.58 to 2.92%, with a decrease of 36.4%. Compared with the normal temperature, the maximum principal strain at 1000 °C is equivalent, with an increase of only 6.5%. In short, the maximum principal strain of sandstone has two peaks at 400 °C and 800 °C, which are closely related to the stress state.

The intermediate principal strain exhibits a unimodal change with increasing temperature (Fig. 7b). As the peak strain is negative, it indicates that the intermediate principal strain undergoes expansive deformation. The absolute value of the peak strain increases and then decreases with increasing temperature. The threshold temperature is 800 °C. In this experiment, the intermediate principal stress plays a role in constraining the deformation of the specimen in that direction. The absolute value of the peak strain in the  $\epsilon_2$  direction of the sandstone ranges from 0.1 to 0.25%, indicating relatively small values. The peak strain in the direction of the minimum principal stress (Fig. 7c) exhibits a bimodal change with increasing temperature, similar to the pattern shown in Fig. 7a. However, the numerical values of the peak strain in the direction of the minimum principal stress are negative, indicating that the specimens undergo expansive deformation in that direction during the failure stage. It should be noted that the two turning points of the peak strain occur at 400 °C and 800 °C, and the strain values are relatively close.

Volumetric strain is the sum of the three principal strains in different directions. The formula (Eq. 1) for volumetric strain is as follows:

$$\epsilon_v = \Delta V/V_0 = \epsilon_1 + \epsilon_2 + \epsilon_3 \quad (1)$$

$\Delta V$  refers to the volume change during compression of the specimen, while  $V_0$  represents the initial volume of the specimen without any applied stress.

Since the direction of the maximum principal stress plays a crucial role and the deformation in the direction of the maximum principal strain is significant, the relationship between volume strain and temperature (Fig. 7d) is controlled by the maximum principal strain, exhibiting a similar pattern as shown in Fig. 7a. The maximum value of the volume strain is 4%, corresponding to 800 °C, indicating that the sandstone can withstand significant volumetric deformation at this temperature. This demonstrates that the deformation characteristics of the coal-bearing sandstone exhibit a strong temperature effect.

According to the International Rock Mechanics Recommendation<sup>55,56</sup>, the slope of the straight line segment in the stress–strain curve is taken as the elastic modulus data, and the relationship between the elastic modulus

of sandstone and temperature is shown in Fig. 8. The elastic modulus increases first and then decreases with the increase in temperature, showing a bimodal phenomenon. The elastic modulus of sandstone is the highest at 400 °C. When the temperature rises from NT to 400 °C, the elastic modulus increases from 5.42 to 6.81 GPa, representing an increase of 25.6%. When the temperature ranges from 400 to 600 °C, the elastic modulus decreases from 6.81 to 6.45 by 5.2%. After reaching 600–800 °C, the elastic modulus of sandstone increases slightly. From 800 to 1000 °C, the elastic modulus of sandstone suddenly drops from 6.60 to 4.63 GPa, with a decrease of 29.8%. Compared with normal temperature, the elastic modulus of sandstone decreases by 14.5% at 1000 °C. In short, the elastic modulus of sandstone reaches the maximum at 400 °C, changes only slightly in the range of 200–800 °C, and drops sharply when the temperature exceeds 800 °C.

**Analysis on strength characters.** The effect of temperature and stress coupling on the peak strength of sandstone under the true triaxial condition is shown in Fig. 9. It can be seen that with the increase in temperature, the average peak strength of sandstone presents a bimodal variation law (Fig. 9). There are two extremes at 400 °C and 800 °C. The strength of sandstone increases continuously from NT to 400 °C, with an increase of 73.5%. After the temperature continues to increase, the strength decreases for the first time, with a decrease of 15.8%. The average peak strength of sandstone reaches the maximum value of 245.45 MPa at 800 °C, and then decreases sharply at 1000 °C, with a decrease of 49.2%.

**AE behavior.** Rock acoustic emission (AE) is the phenomenon of transient elastic waves caused by lattice dislocation or micro-crack propagation in the process of the loading and deformation of rock materials. Previous studies have shown that micro-cracking is the main cause of acoustic emission activity of sandstone<sup>57</sup>. Figure 10 shows the number of AE events and the variation of differential stress with axial strain during the failure of sandstone specimens under TTT conditions ( $\sigma_3 = 10$  MPa and  $\sigma_2 = 20$  MPa).

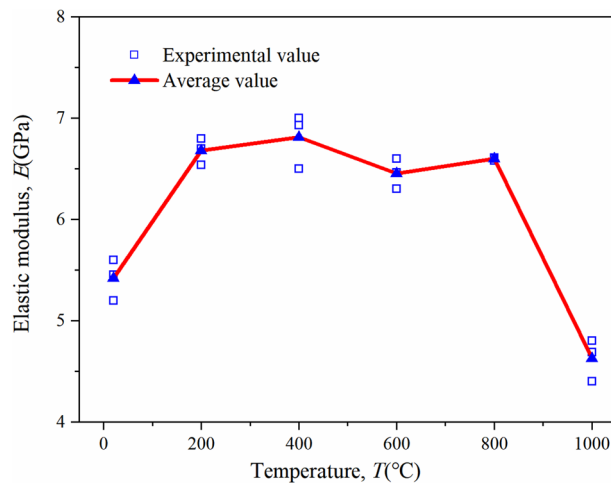


**Figure 8.** Temperature dependence of modulus of elasticity of sandstone.

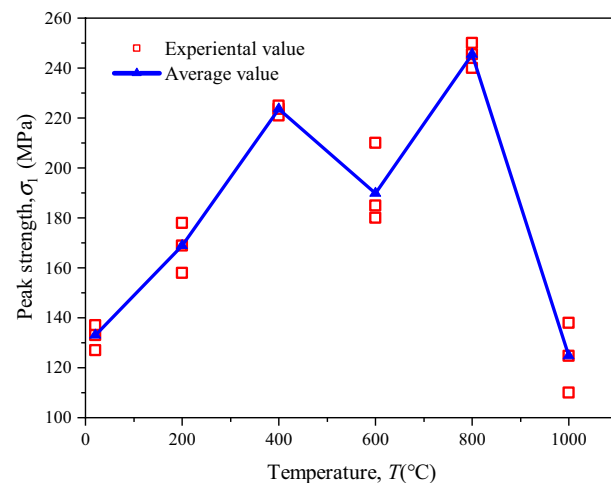


**Figure 9.** Temperature dependence of peak stress.



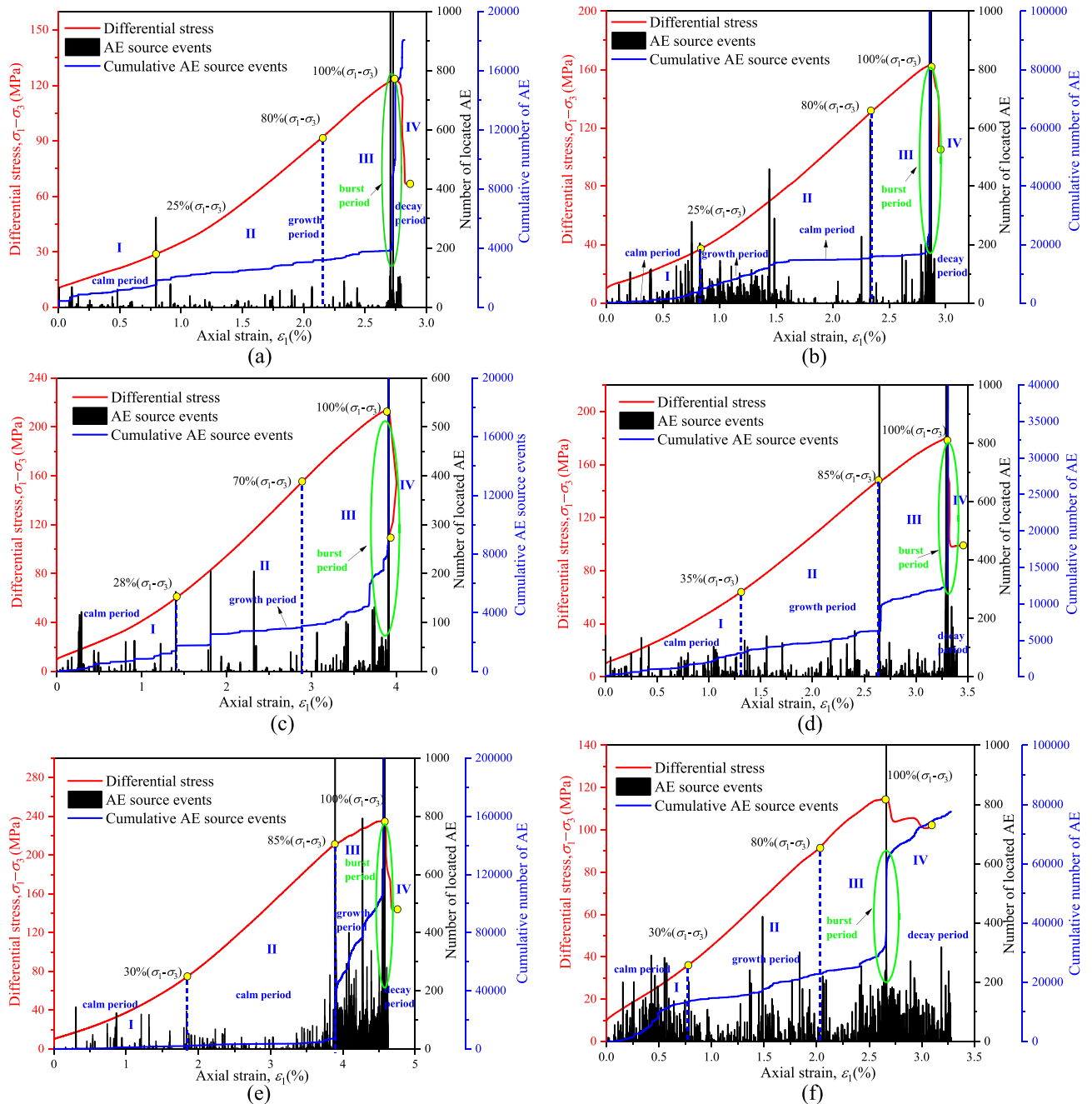


**Figure 10.** Variation in the differential stress and number of acoustic emission events with axial strain under true triaxial conditions at different temperatures. (a) NT, (b) 200 °C, (c) 400 °C, (d) 600 °C, (e) 800 °C and (f) 1000 °C.

From the above test results, it can be seen that the sample has obvious acoustic emission phenomenon in the test, and the number of acoustic emission is taken as the index of acoustic emission activity in the analysis. According to the stage division of the damage evolution process of sandstone in the true triaxial state, stage II (stable propagation stage of microcracks) begins with the first significant increase in stress in the acoustic emission signal, which is about 25–35% of the peak differential stress; Stage III (unstable microcrack propagation stage) begins with the second sharp increase in the acoustic emission signal stress<sup>58,59</sup>, which is about 70%–90% of the peak differential stress. When the stress reaches 25–35% of the strength limit, the acoustic emission activity becomes clearly strengthened for the first time, which indicates the generation of microscopic cracks in rock. When the stress reaches 70–90% of the strength limit, the acoustic emission counting rate reaches the maximum, which leads to the appearance of fracture surfaces in rock.

Acoustic emission cumulative counts exhibit distinct stages, which can also be divided into the following four periods based on the slope changes of the cumulative curve: calm period, growth period, burst period, and decay period. The initial compaction stage is the quiet period. There are different degrees of AE activities, but there are few AE events. The early compaction stage can be understood as the gradual closure of some original cracks in

rock under this low stress level, and AE events will occur during the closure process, but the energy is not high, and it has great randomness and fluctuation. After entering the elastic stage, the acoustic emission activity is still relatively low. However, later in the elastic stage, the activity of AE gradually increases, and occasionally a larger level of AE is produced. With the gradual increase in stress, the activity of AE gradually increases, resulting in some AE events with higher energy, mainly because cracks in some areas inside the specimen begin to slip, referred to as the growth stage. With the increase in the load, cracks in the specimen are gradually produced, and more acoustic emission phenomena are produced. When the peak intensity is reached, most of the acoustic emission numbers reach the maximum value, which is called the burst period. As the specimen continues to compress into the residual strength, the acoustic emission rate decreases gradually, indicating that macroscopic cracks have appeared in the specimen, and this stage is part of the decline stage. However, as can be seen from Figure f, there are many events in the quiet period of the sample after a 1000 °C high temperature, which indicates that the cracks on the rock surface expand further when they begin to compress, and gradually form new cracks. When multiple cracks form and penetrate gradually, a macroscopic fracture surface is finally formed.

**Macroscopic fracture characteristics of sandstone.** The failure modes of sandstone specimens under true triaxial conditions at different temperatures are shown in Fig. 11.

The failure modes of the specimens at different temperatures are similar to those of other true triaxial loading<sup>49,53,60,61</sup>, showing an inverted “Y” or an inverted “N” (see Fig. 11). With the increase in the maximum principal stress, the shear stress and the tensile strain parallel to the minimum principal stress on the oblique section of the rock gradually increase. The failure of rock is the relative displacement between rock mineral particles under the action of shear stress or tensile strain on the oblique section. The failure mode of the rock is tensile failure or shear failure, and it depends on the shear stress or tensile strain on the section reaching its limit value.

When the temperature is below 400 °C, the failure mode of the specimen is shear failure, which is caused by the shear stress on the failure surface reaching the limit value. When the temperature exceeds 600 °C, some specimens show shear-tension failure, which is caused by the tensile strain along the direction of the minimum principal stress, reaching its limit value under the action of maximum principal stress. The failure surface is rough and parallel to the minimum principal stress action surface. When failure occurs, it is similar to rock burst and flake peeling takes place, which is a characteristic of tensile failure.

Generally, there are two failure cracks in true triaxial sample, and the minimum fracture angle is taken for analysis. The minimum rupture angle of the specimen at different temperatures is shown in Fig. 12. With the increase in temperature, the fracture angle of samples increases first and then decreases. When the temperature is 800 °C, the maximum rupture angle is 80 °C, and the rupture angle increases by 13 °C compared with normal temperature.

## Discussion

**Relationship between peak stress and temperature.** The mechanical properties of high-temperature sandstones have been extensively studied by various researchers (Fig. 13). Hajpál and Török<sup>62</sup> investigated the Cottaer sandstone in Germany and found a threshold temperature of 750 °C for the uniaxial compression strength. Zhang et al.<sup>32</sup> conducted real-time high-temperature uniaxial compression tests on Xuzhou sandstone and identified a threshold temperature of 600 °C. Dong et al.<sup>15</sup> and Ranjith et al.<sup>22</sup> also observed similar peak strengths corresponding to threshold temperatures in their studies. Yang et al.<sup>28</sup> performed conventional triaxial tests on Rizhao sandstone and found a threshold temperature of 300 °C with a peak strength of 10 MPa under peritectic compression. Li et al.<sup>42</sup> conducted true triaxial tests on Sichuan quartz-rich sandstone after high-temperature treatment and observed a bimodal change in peak strength with increasing temperature, with a threshold temperature of 800 °C. The temperature thresholds for the bimodal variation are 400 °C and 800 °C in the text, while the sandstone at 800 °C represents the point of maximum strength in the single-peak variation. The effect of high temperature on sandstone strength is attributed to thermal stress resulting from mineral grain expansion and increased frictional resistance caused by dehydration. We observed a slight degradation in the

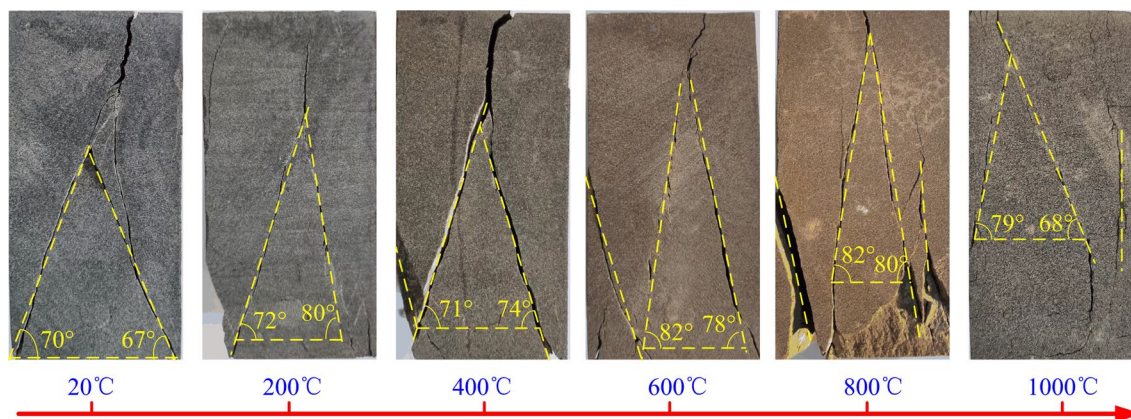


**Figure 11.** Damage pattern of specimens at different temperatures.

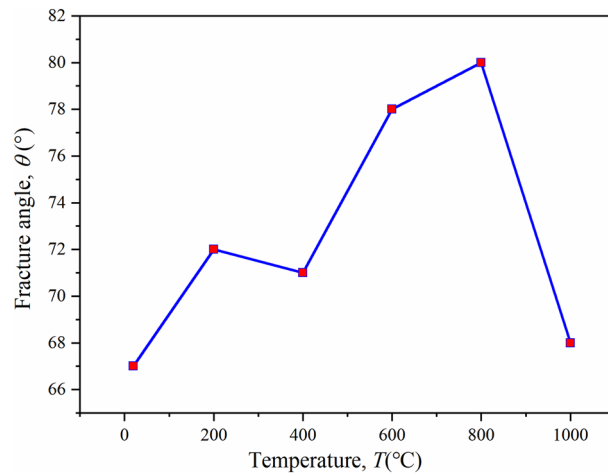


**Figure 12.** Minimum angle of fracture of specimens at different temperatures.

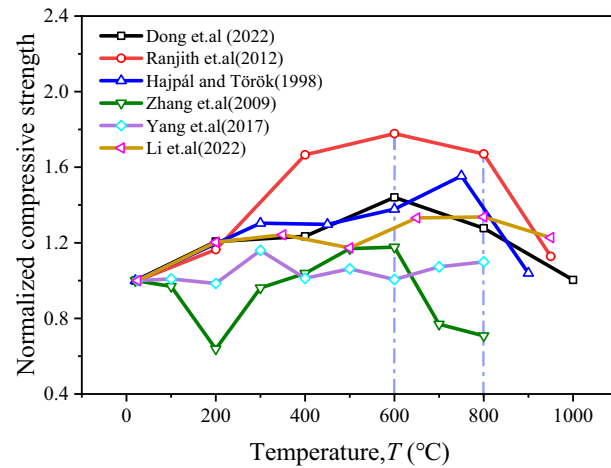


**Figure 13.** Peak strength of high-temperature sandstone as a function of temperature.

mechanical strength of sandstone when subjected to temperatures of up to 600 °C. The peak stress decreased by approximately 15% compared to 400 °C conditions. Additionally, an increase in crack density was observed above 600 °C, primarily due to the  $\alpha$ - $\beta$  transformation of quartz. Furthermore, the study highlighted the influence of microstructural features (Fig. 14), including mineralogy and grain size distribution, on the high-temperature mechanical characteristics of sandstone. We found that the rock's microstructure played a crucial role in determining its response to thermal loading.

These findings further contribute to the understanding of how high temperatures influence the strength characteristics of sandstone and highlight the importance of considering both temperature and stress state in assessing its mechanical behavior.

**Temperature-moisture variation in sandstone.** Based on the analysis of the above experimental results, the main mechanism of the change of sandstone mechanical properties after high temperature treatment includes water loss and structural damage caused by thermal reaction. The mass loss of sandstone is mainly manifested through the evaporation of water, and it is commonly characterized by the term “loss-on-ignition” (LOI). In this study, the LOI is defined as the ratio of the mass loss due to high temperature evaporation to the mass of the sample before heating, expressed as a percentage by Eq. (2).

$$LOI = [(m_{s1} - m_{s2}) / m_{s1}] \times 100\% \quad (2)$$

where  $m_{s1}$  is the initial mass of the sample before high-temperature testing, and  $m_{s2}$  is the mass of the sample after heating and volatilization.

The relationship between sandstone mass loss and temperature is shown in Fig. 15. When the sandstone sample is heated to 200 °C, the quality of sandstone decreases slightly under the influence of thermal expansion and free water evaporation. Based on the quality of rocks after high-temperature treatment, the LOI of sandstone is

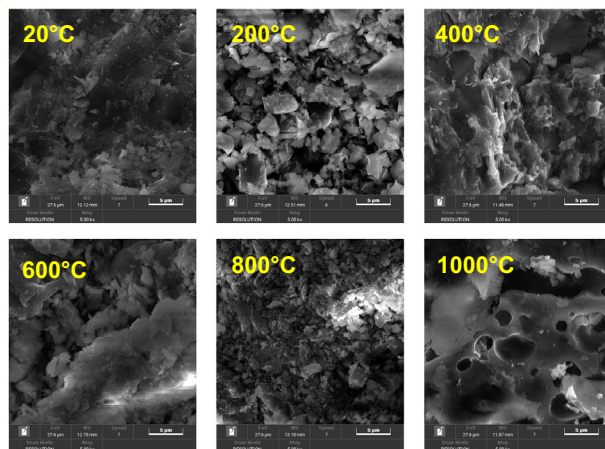


**Figure 14.** SEM image of high temperature sandstone.

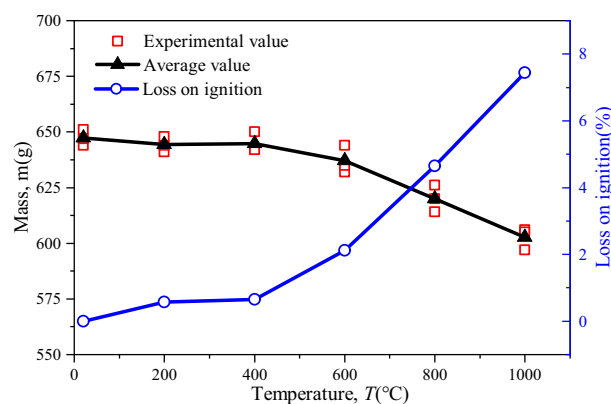


**Figure 15.** Relationship between mass loss of sandstone and temperature.

0.58%, and the overall rock mechanical parameters are improved due to the compaction of pores. At 200–400 °C, the LOI of sandstone is only 0.65%, which is very close to the results at 200 °C. When the sandstone sample is heated to 400–600 °C, some minerals in the sandstone are ablated, the bound water in the sandstone is lost, and the defects increase. In addition, organic matter such as carbon and sulfur will undergo thermal decomposition and other thermochemical reactions, which will further reduce the rock quality. The LOI of sandstone is 2.11%, which is about 3.7 times of the LOI at 200 °C. At the same time, as the temperature approaches 600 °C, the quartz transforms from the  $\alpha$  phase to  $\beta$  phase<sup>59</sup>, during which the volume expands slightly and impurities in the quartz crystal are purified. This transformation causes great changes in the physical and mechanical properties of sandstone, which shows that the peak compressive strength of sandstone decreases by about 15% compared with 400 °C. At the stage of 600–800 °C, many minerals in sandstone begin to melt and phase changes occur, the LOI further increases to 4.65%, some minerals are ablated, the rock quality decreases continuously. When the sandstone sample is heated to 800–1000 °C, some minerals in the sample melt, resulting in many microscopic defects in the rock, among which the thermal reaction of clay minerals is enhanced, minerals are rearranged, the edges and corners of mineral particles disappear, the morphology of pores and cracks changes obviously, and even macroscopic cracks occur. The true triaxial compressive strength of sandstone decreases rapidly, and the peak strength is close to the true triaxial strength at NT.

### Conclusions and suggestions

In this study, a series of true triaxial tests (TTT) were carried out on coal-measure sandstone with a self-developed true triaxial test system combined with acoustic emission (AE) monitoring, and the mass loss, deformation characteristics and failure modes of sandstone before and after heat treatment were systematically studied. The main results of this study can be summarized as follows:

- (1) The true triaxial mechanical properties of sandstone after high temperature treatment are closely related to temperature, and the peak strength, maximum principal strain, minimum fracture angle and elastic modulus all show bimodal changes, not single peak changes shown by uniaxial compression and triaxial compression. The following rules are observed: the first peak strength appears from RT to 400 °C, and the



- second peak appears from 600 to 1000 °C. When the temperature rises to 800 °C, the sandstone reaches the peak strength of the high temperature test. At the same time, the maximum principal strain, minimum fracture Angle and volume strain also reach the peak, and 400 °C is the transition temperature of the elastic modulus.
- (2) The true triaxial high temperature sandstone test results are in good agreement with the existing true triaxial theory and experimental results. The failure modes of samples at different temperatures are inverted “Y” or inverted “N”. Shear failure occurs when the temperature is below 400 °C, and shear-tension failure occurs when the temperature is over 600 °C. There are four periods of AE signaling, namely the quiet period, growth period, burst period and decline period, and the number of AE events corresponds to the deviator stress interval.
  - (3) By changing the heat-treatment temperature of the rock, it can be found that the strength and physical properties of rock change substantially and irreversibly after heating. The average peak strength of the sandstone reaches its maximum value at 800 °C, which is an increase of 84.2% compared to room temperature. Compared to 400 °C, there is an increase of 9.8%. However, at a temperature of 1000 °C, there is a sharp decrease in peak strength, with a decrease of 49.2%.

## Data availability

The data used to support the findings and results of this study are available from the corresponding author upon request.

Received: 1 April 2023; Accepted: 8 August 2023

Published online: 10 August 2023

## References

1. Hudson, J. A., Stephansson, O., Andersson, J., Tsang, C. F. & Jing, L. Coupled T-H-M issues relating to radioactive waste repository design and performance. *Int. J. Rock Mech. Min. Sci.* **38**, 143–161. [https://doi.org/10.1016/s1365-1609\(00\)00070-8](https://doi.org/10.1016/s1365-1609(00)00070-8) (2001).
2. Atrens, A. D., Gurgenci, H. & Rudolph, V. CO<sub>2</sub> Thermosiphon for competitive geothermal power generation. *Energy Fuels* **23**, 553–557. <https://doi.org/10.1021/ef800601z> (2009).
3. Al-Zareer, M., Dincer, I. & Rosen, M. A. Analysis and assessment of a hydrogen production plant consisting of coal gasification, thermochemical water decomposition and hydrogen compression systems. *Energy Convers. Manag.* **157**, 600–618. <https://doi.org/10.1016/j.enconman.2017.11.047> (2018).
4. Kapusta, K., Wiatowski, M., Stańczyk, K., Zagorak, R. & Thomas, H. R. Large-scale experimental investigations to evaluate the feasibility of producing methane-rich gas (SNG) through underground coal gasification process. Effect of coal rank and gasification pressure. *Energies* **13**, 1–14. <https://doi.org/10.3390/en13061334> (2020).
5. Klebingat, S., Kempka, T., Schulten, M., Azzam, R. & Fernandez-Steeger, T. M. Optimization of synthesis gas heating values and tar by-product yield in underground coal gasification. *Fuel* **229**, 248–261. <https://doi.org/10.1016/j.fuel.2018.02.039> (2018).
6. Perkins, G. Underground coal gasification—Part I: Field demonstrations and process performance. *Prog. Energy Combust. Sci.* **67**, 158–187. <https://doi.org/10.1016/j.peccs.2018.02.004> (2018).
7. Liu, Y., Wang, G., Yue, G., Lu, C. & Zhu, X. Impact of CO<sub>2</sub> injection rate on heat extraction at the HDR geothermal field of Zhacangou, China. *Environ. Earth Sci.* **76**, 1–11. <https://doi.org/10.1007/s12665-017-6551-7> (2017).
8. Lu, C., Lin, W. J., Gan, H. N., Liu, F. & Wang, G. L. Occurrence types and genesis models of hot dry rock resources in China. *Environ. Earth Sci.* **76**, 1–19. <https://doi.org/10.1007/s12665-017-6947-4> (2017).
9. Mogi, K. Fracture and flow of rocks under high triaxial compress. *J. Geophys. Res.* **76**, 1255–1269 (1971).
10. Najm, S. J. & Daraei, A. Forecasting and controlling two main failure mechanisms in the Middle East's longest highway tunnel. *Eng. Fail. Anal.* **146**, 1–15. <https://doi.org/10.1016/j.engfailanal.2023.107091> (2023).
11. Zuo, J. P., Xie, H. P., Zhou, H. W. & Peng, S. P. SEM in situ investigation on thermal cracking behaviour of Pingdingshan sandstone at elevated temperatures. *Geophys. J. Int.* <https://doi.org/10.1111/j.1365-246X.2010.04532.x> (2010).
12. Peng, J., Rong, G., Tang, Z. & Sha, S. Microscopic characterization of microcrack development in marble after cyclic treatment with high temperature. *Bull. Eng. Geol. Environ.* **78**, 5965–5976. <https://doi.org/10.1007/s10064-019-01494-2> (2019).
13. Freire-Lista, D. M., Fort, R. & Varas-Muriel, M. J. Thermal stress-induced microcracking in building granite. *Eng. Geol.* **206**, 83–93. <https://doi.org/10.1016/j.enggeo.2016.03.005> (2016).
14. Pathiranagei, S. V., Gratchev, I. & Kong, R. Engineering properties of four different rocks after heat treatment. *Geomech. Geophys. Geo-Energy Geo-Resour.* **7**, 1–21. <https://doi.org/10.1007/s40948-020-00211-8> (2021).
15. Dong, Z. *et al.* Evaluation of thermophysical and mechanical properties of sandstone due to high-temperature. *Materials (Basel)* **15**, 1–13. <https://doi.org/10.3390/ma15238692> (2022).
16. Zhang, Y. *et al.* Pore characteristics and mechanical properties of sandstone under the influence of temperature. *Appl. Therm. Eng.* **113**, 537–543. <https://doi.org/10.1016/j.applthermaleng.2016.11.061> (2017).
17. Hassanzadegan, A., Blöcher, G., Milsch, H., Urpi, L. & Zimmermann, G. The effects of temperature and pressure on the porosity evolution of Flechtinger sandstone. *Rock Mech. Rock Eng.* **47**, 421–434. <https://doi.org/10.1007/s00603-013-0401-z> (2013).
18. Hajpál, M. Changes in sandstones of historical monuments exposed to fire or high temperature. *Fire Technol.* **38**, 373–382 (2002).
19. Zhang, Y., Ma, Y., Gu, B., Ta, X. & Wang, Q. Uniaxial compressive strength and failure characteristics of arkosic sandstone after thermal treatment. *Therm. Sci.* **24**, 2991–3000. <https://doi.org/10.2298/tsci180909026z> (2020).
20. Sun, Q. *et al.* Thermal properties of sandstone after treatment at high temperature. *Int. J. Rock Mech. Min. Sci.* **85**, 60–66 (2016).
21. Lei, R. *et al.* The evolution of sandstone microstructure and mechanical properties with thermal damage. *Energy Sci. Eng.* **7**, 3058–3075. <https://doi.org/10.1002/ese3.480> (2019).
22. Ranjith, P. G., Viete, D. R., Bai, J. C. & Perera, M. Transformation plasticity and the effect of temperature on the mechanical behaviour of Hawkesbury sandstone at atmospheric pressure. *Eng. Geol.* **151**, 120–127. <https://doi.org/10.1016/j.enggeo.2012.09.007> (2012).
23. Shi, X. *et al.* Investigation on physical and mechanical properties of bedded sandstone after high-temperature exposure. *Bull. Eng. Geol. Environ.* **79**, 2591–2606. <https://doi.org/10.1007/s10064-020-01729-7> (2020).
24. Liu, S. & Xu, J. An experimental study on the physico-mechanical properties of two post-high-temperature rocks. *Eng. Geol.* **185**, 63–70. <https://doi.org/10.1016/j.enggeo.2014.11.013> (2015).
25. Sirdesai, N. N., Singh, T. N., Ranjith, P. G. & Singh, R. Effect of varied durations of thermal treatment on the tensile strength of red sandstone. *Rock Mech. Rock Eng.* **50**, 1–9. <https://doi.org/10.1007/s00603-016-1047-4> (2016).

26. Yang, Y., Wei, S., Zhang, J., Wu, J. & Zhang, C. Effect study of heat treatment on tensile properties of coarse sandstone. *Sci. Rep.* **12**, 1–12. <https://doi.org/10.1038/s41598-022-21164-w> (2022).
27. Liu, K. *et al.* Effects of thermal treatment on the shear behavior and characteristics of intact sandstone: Laboratory experiment of variable-angle shear. *Bull. Eng. Geol. Environ.* **81**, 1–21. <https://doi.org/10.1007/s10064-022-02973-9> (2022).
28. Yang, S. Q., Xu, P., Li, Y. B. & Huang, Y. H. Experimental investigation on triaxial mechanical and permeability behavior of sandstone after exposure to different high temperature treatments. *Geothermics* **69**, 93–109. <https://doi.org/10.1016/j.geothermics.2017.04.009> (2017).
29. Wang, X. *et al.* Experimental study on mechanical properties of gas storage sandstone and its damage under temperature and pressure. *Front. Earth Sci.* **10**, 1–11. <https://doi.org/10.3389/feart.2022.905642> (2022).
30. Kumari, W. G. P., Ranjith, P. G., Perera, M. S. A., Chen, B. K. & Abdulgatov, I. M. Temperature-dependent mechanical behaviour of Australian Strathbogie granite with different cooling treatments. *Eng. Geol.* **229**, 31–44. <https://doi.org/10.1016/j.enggeo.2017.09.012> (2017).
31. Dong, Z., Sun, Q. & Ranjith, P. G. Surface properties of grayish-yellow sandstone after thermal shock. *Environ. Earth Sci.* **78**, 1–13. <https://doi.org/10.1007/s12665-019-8451-5> (2019).
32. Zhang, L., Mao, X. & Lu, A. Experimental study on the mechanical properties of rocks at high temperature. *Sci. China Ser. E Technol. Sci.* **52**, 641–646. <https://doi.org/10.1007/s11431-009-0063-y> (2009).
33. Rao, Q., Wang, Z., Xie, H. & Xie, Q. Experimental study of mechanical properties of sandstone at high temperature. *J. Cent. South Univ. Technol.* **14**, 478–483. <https://doi.org/10.1007/s11771-007-0311-x> (2007).
34. Liu, Q., Qian, Z. & Wu, Z. Micro/macro physical and mechanical variation of red sandstone subjected to cyclic heating and cooling: An experimental study. *Bull. Eng. Geol. Environ.* **78**, 1485–1499. <https://doi.org/10.1007/s10064-017-1196-z> (2017).
35. Li, Q., Yin, T., Li, X. & Zhang, S. Effects of rapid cooling treatment on heated sandstone: A comparison between water and liquid nitrogen cooling. *Bull. Eng. Geol. Environ.* **79**, 313–327. <https://doi.org/10.1007/s10064-019-01571-6> (2019).
36. Ghobadi, M. H. & Babazadeh, R. Experimental studies on the effects of cyclic freezing–thawing, salt crystallization, and thermal shock on the physical and mechanical characteristics of selected sandstones. *Rock Mech. Rock Eng.* **48**, 1001–1016. <https://doi.org/10.1007/s00603-014-0609-6> (2014).
37. Mahanta, B., Ranjith, P. G., Vishal, V. & Singh, T. N. Temperature-induced deformational responses and microstructural alteration of sandstone. *J. Pet. Sci. Eng.* **192**, 593–603. <https://doi.org/10.1016/j.petrol.2020.107239> (2020).
38. Liu, Z., Yao, Q., Kong, B. & Yin, J. Macro-micro mechanical properties of building sandstone under different thermal damage conditions and thermal stability evaluation using acoustic emission technology. *Constr. Build. Mater.* **246**, 1–11. <https://doi.org/10.1016/j.conbuildmat.2020.118485> (2020).
39. Kong, B. *et al.* Electromagnetic radiation characteristics and mechanical properties of deformed and fractured sandstone after high temperature treatment. *Eng. Geol.* **209**, 82–92. <https://doi.org/10.1016/j.enggeo.2016.05.009> (2016).
40. Zhang, G. *et al.* Effects of uniaxial and triaxial compression tests on the frozen sandstone combining with CT scanning. *Int. J. Phys. Model. Geotech.* **19**, 261–274. <https://doi.org/10.1680/jphmg.18.00006> (2019).
41. Chen, G. Q., Zhang, Y. & Li, Y. Thermal-acoustic precursor information chain of rock failure under true triaxial loading. *Chin. J. Geotech. Eng.* **40**, 1–13 (2021).
42. Li, X. *et al.* Influence of high-temperature treatment on strength and failure behaviors of a quartz-rich sandstone under true triaxial condition. *Lithosphere* <https://doi.org/10.2113/2022/3086647> (2022).
43. Wang, H., Dyskin, A. & Pasternak, E. Comparative analysis of mechanisms of 3-D brittle crack growth in compression. *Eng. Fail. Anal.* <https://doi.org/10.1016/j.engfracmech.2019.106656> (2019).
44. Haimson, B. The hydrofracturing stress measuring method and recent field results. *Int. J. Rock Mech. Min. Sci. Geomech. Abstr.* **15**, 167–178 (1978).
45. Haimson, B. & Chang, C. A new true triaxial cell for testing mechanical properties of rock, and its use to determine rock strength and deformability of Westerly granite. *Int. J. Rock Mech. Min. Sci.* **37**, 285–296. [https://doi.org/10.1016/s1365-1609\(99\)00106-9](https://doi.org/10.1016/s1365-1609(99)00106-9) (2000).
46. Chang, C. & Haimson, B. True triaxial strength and deformability of the German Continental Deep Drilling Program (KTB) deep hole amphibolite. *J. Geophys. Res. Solid Earth* **105**, 18999–19013. <https://doi.org/10.1029/2000jb900184> (2000).
47. Al-Ajmi, A. M. & Zimmerman, R. W. Relation between the Mogi and the Coulomb failure criteria. *Int. J. Rock Mech. Min. Sci.* **42**, 431–439 (2005).
48. Al-Ajmi, A. M. & Zimmerman, R. W. Stability analysis of vertical boreholes using the Mogi–Coulomb failure criterion. *Int. J. Rock Mech. Min. Sci.* **43**, 1200–1211. <https://doi.org/10.1016/j.ijrmm.2006.04.001> (2006).
49. Li, Z. L. *et al.* Experimental investigation on true triaxial deformation and progressive damage behaviour of sandstone. *Sci. Rep.* **9**, 1–19. <https://doi.org/10.1038/s41598-019-39816-9> (2019).
50. Lu, Y. L. *et al.* Damage evolution and failure behavior of sandstone under true triaxial compression. *Geotech. Test. J.* **42**, 610–637. <https://doi.org/10.1520/gtj20170295> (2019).
51. Ding, K. *et al.* Experimental study on relative permeability characteristics for CO<sub>2</sub> in sandstone under high temperature and overburden pressure. *Minerals* **11**, 1–13. <https://doi.org/10.3390/min11090956> (2021).
52. Chandelle, V. *et al.* Underground coal gasification on the Thulin site: Results of analysis from post-burn drillings. *Fuel* **72**, 949–963. [https://doi.org/10.1016/0016-2361\(93\)90292-A](https://doi.org/10.1016/0016-2361(93)90292-A) (1993).
53. Li, W. S., Wang, L. G. & Lu, Y. L. Experimental investigation on the strength, deformation and failure characteristics of sandstone under true triaxial compression. *J. Min. Saf. Eng.* **36**, 191–197 (2019).
54. Wang, S. *et al.* An Experimental study on the effects of true triaxial loading and unloading stress paths on the mechanical properties of red sandstone. *Minerals* **12**, 1–14. <https://doi.org/10.3390/min12020204> (2022).
55. Brown, E. T. *Rock Characterization, Testing & Monitoring: ISRM Suggested Methods* (International Society for Rock Mechanics by Pergamon Press, 1981).
56. Fairhurst, C. E. & Hudson, J. A. Draft ISRM suggested method for the complete stress-strain curve for intact rock in uniaxial compression. *Int. J. Rock Mech. Min. Sci.* **36**, 279–289 (1999).
57. Wu, X. Y., Baud, P. & Wong, T.-F. Micromechanics of compressive failure and spatial evolution of anisotropic damage in Darley Dale sandstone.pdf. *Int. J. Rock Mech. Min. Sci.* **37**, 143–160 (2000).
58. Eberhardt, E., Stead, D., Stimpson, B. & Read, R. S. Identifying crack initiation and propagation thresholds in brittle rock. *Can. Geotech. J.* **35**, 222–233. <https://doi.org/10.1139/t97-091> (1998).
59. Martin, C. D. & Chandler, N. A. The progressive fracture of Lac du Bonnet granite. *Int. J. Rock Mech. Min. Sci.* **31**, 643–659. [https://doi.org/10.1016/0148-9062\(94\)90005-1](https://doi.org/10.1016/0148-9062(94)90005-1) (1994).
60. Ma, X. & Haimson, B. C. Failure characteristics of two porous sandstones subjected to true triaxial stresses. *J. Geophys. Res. Solid Earth* **121**, 6477–6498. <https://doi.org/10.1002/2016jb012979> (2016).
61. Ma, X., Rudnicki, J. W. & Haimson, B. C. Failure characteristics of two porous sandstones subjected to true triaxial stresses: Applied through a novel loading path. *J. Geophys. Res. Solid Earth* **122**, 2525–2540. <https://doi.org/10.1002/2016jb013637> (2017).
62. Hajpál, M. & Török, Á. Petrophysical and mineralogical studies of burnt sandstones. In *2nd Int. PhD Symposium in Civil Engineering 1998 Budapest* 1–9 (1998).

## Acknowledgements

The authors would like to acknowledge the editor for their valuable comments that helped with the improvement of this paper.

## Author contributions

S.W. wrote the main manuscript text, B.R. finished test, C.J. prepared Figs. 1, 2, 3, 12, 13, 14 and 15. K.D. prepared Figs. 4, 5, 6, 7, 8, 9, 10 and 11. J.G. completed the translation of the manuscript. L.W. provided the ideas and general guidance for the article. All authors reviewed the manuscript.

## Competing interests

The authors declare no competing interests.

## Additional information

**Correspondence** and requests for materials should be addressed to L.W.

**Reprints and permissions information** is available at [www.nature.com/reprints](http://www.nature.com/reprints).

**Publisher's note** Springer Nature remains neutral with regard to jurisdictional claims in published maps and institutional affiliations.



**Open Access** This article is licensed under a Creative Commons Attribution 4.0 International License, which permits use, sharing, adaptation, distribution and reproduction in any medium or format, as long as you give appropriate credit to the original author(s) and the source, provide a link to the Creative Commons licence, and indicate if changes were made. The images or other third party material in this article are included in the article's Creative Commons licence, unless indicated otherwise in a credit line to the material. If material is not included in the article's Creative Commons licence and your intended use is not permitted by statutory regulation or exceeds the permitted use, you will need to obtain permission directly from the copyright holder. To view a copy of this licence, visit <http://creativecommons.org/licenses/by/4.0/>.

© The Author(s) 2023